DES AND RANS SIMULATIONS OF DELTA WING VORTICAL FLOWS

Scott Morton[*], James Forsythe[&], Anthony Mitchell[φ], and David Hajek[∞]
United States Air Force Academy, Department of Aeronautics_
2410 Faculty Drive, Suite 108
USAF Academy, CO 80840-6400, USA.

ABSTRACT

An understanding of the vortical structures and vortex breakdown is essential for the development of highly maneuverable and high angle of attack flight. This is primarily due to the physical limits these phenomena impose on aircraft and missiles at extreme flight conditions. Demands for more maneuverable air vehicles have pushed the limits of current CFD methods in the high Reynolds number regime. Simulation methods must be able to accurately describe the unsteady, vortical flowfields associated with fighter aircraft at Reynolds numbers more representative of full scale vehicles. It is the goal of this paper to demonstrate the ability of Detached-Eddy Simulation, a hybrid RANS-LES method, to accurately predict vortex breakdown at Reynolds numbers above 1 million. Very detailed experiments performed at Onera with LDV and pressure measurement are used to compare simulations utilizing both RANS and DES turbulence models.

INTRODUCTION

The delta wing flow field is dominated by vortical structures, the most prominent called leading-edge vortices. As angle of attack increases, these leading-edge vortices experience a sudden disorganization, known as vortex breakdown which can be described by a rapid deceleration of both the axial and swirl components of the mean velocity and, at the same time, a dramatic expansion of the vortex core. Henri Werlé first photographed the vortex breakdown phenomenon in 1954, during water tunnel tests of a slender delta wing model at Onera.[1] This work was quickly confirmed by Peckham and Atkinson,[2] Elle[3] and Lambourne and Bryer[4] and spawned a large number of experimental, computational and theoretical studies which continue today. These investigations led to the development of several theories governing vortex breakdown, although none have been universally accepted.[5-9] Despite this lack of a unified theoretical interpretation, several forms of vortex breakdown have been identified[7,10] (i.e. bubble, helical, etc.), and the global characteristics of the phenomena are understood. During the breakdown process, the mean axial velocity component rapidly decreases until it reaches a stagnation point and/or becomes negative on the vortex axis. This stagnation point, called the breakdown location, is unsteady and typically oscillates about some mean position along the axis of the vortex core[11,12] (see Fig. 1). As angle of attack is increased, the mean vortex breakdown location moves upstream over the delta wing (from the trailing edge toward the apex).

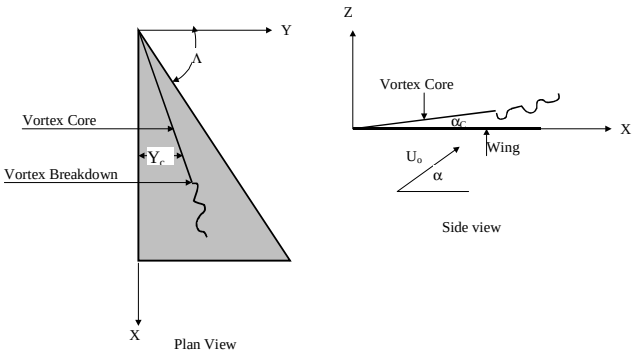

Figure 1: Definition of the spatial location of the vortex core and the vortex breakdown location.

The primary vortex over a slender delta wing at angle of attack is principally inviscid. Unfortunately, the location of the vortex is strongly affected by a secondary vortex formed by the inter-relationship between the surface boundary layer and the primary vortex. In addition, the vortex breakdown phenomenon creates turbulent kinetic energy that must be modeled properly. Many turbulence models create orders of magnitude too much turbulent edyy viscosity in the primary vortex core which significantly alters the flowfield and in some case eliminates breakdown observed experimentally at high Reynolds numbers. For these reasons, an accurate prediction of the flowfield over a slender delta wing at high angles of attack and high Reynolds numbers must model the boundary layer, primary and secondary vortex, and turbulent kinetic energy correctly.

While advances have taken place in areas such as grid generation and fast algorithms for solutions of systems of equations, CFD has remained limited as a reliable tool for prediction of inherently unsteady flows at flight Reynolds numbers. Current engineering approaches to prediction of unsteady flows are based on solution of the Reynolds-averaged Navier-Stokes (RANS) equations. The turbulence models employed in RANS methods necessarily model the entire spectrum of turbulent motions. While often adequate in steady flows with no regions of reversed flow, or possibly exhibiting shallow separations, it appears inevitable that RANS turbulence models are unable to accurately predict phenomena

dominating flows characterized by massive separations. Unsteady massively separated flows are characterized by geometry-dependent and three dimensional turbulent eddies. These eddies, arguably, are what defeats RANS turbulence models, of any complexity.

To overcome the deficiencies of RANS models for predicting massively separated flows, Spalart et.al.[13,20] proposed Detached-Eddy Simulation (DES) with the objective of developing a numerically feasible and accurate approach combining the most favorable elements of RANS models and Large Eddy Simulation (LES). The primary advantage of DES is that it can be applied at high Reynolds numbers as can Reynolds-averaged techniques, but also resolves geometry-dependent, unsteady three-dimensional turbulent motions as in LES. DES predictions to date have been favorable, forming one of the motivations for this research. The specific aim of this work is to apply and assess DES to the problem of vortex breakdown over slender delta wings at high Reynolds number.

NUMERICAL METHOD

In this section a brief description of the numerical method is provided. Full details of the computational scheme and the solution method are presented in Refence [14]. The delta wing model used is Onera's sharp-edged, 70° sweep angle (Λ) delta wing with a root chord (c) of 950mm (Fig. 2). The model has a wingspan of 691.5mm at its trailing edge, is 20mm thick, and is beveled on the windward side at an angle of 15° to form a sharp leading edge. Solutions were obtained for a freestream velocity of 24 m/s, an angle of attack of 27 deg, and a freestream pressure and temperature resulting in a Reynolds number of 1.56 million. Angle of attack, Reynolds number and Mach number were chosen to match the wind tunnel data.

Solutions were computed with the September 2001 version of Cobalt developed by Cobalt Solutions. Cobalt solves the unsteady, three-dimensional, compressible Navier-Stokes equations on an unstructured grid. The code has several choices of turbulence models including Spalart Almaras (SA), SA with rotation corrections (SARC), and SST RANS, as well as DES versions of SA and SST. The computational mesh currently being used is a 2.45 million cell unstructured mesh generated with the software packages GridTool[15] and VGRIDns[16]. It consists of an inner region of prisms for the boundary layer with a y+ less than 1 and an outer region of tetrahedrons. Fig. 2 depicts the delta wing grid used for this study. As is evident in the figure, cells are clustered in the boundary layer and in the region of the vortex core. Also, the grid represents only the half-span of the delta wing.

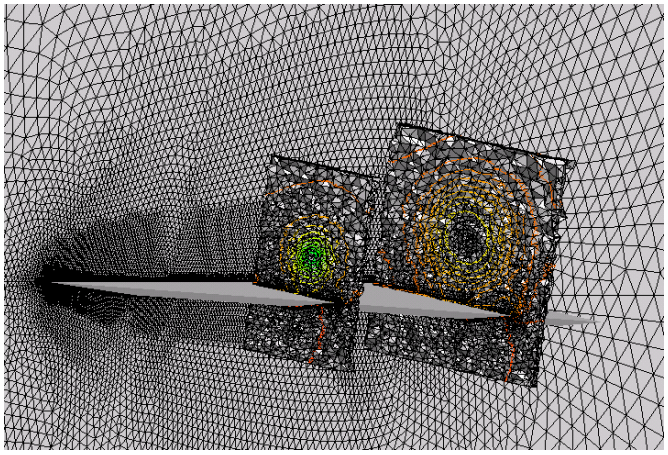

Figure 2: Unstructured Prism/Tetrahedron Grid, 2.47M Cells.

Governing Equations

The Navier-Stokes equations are solved in an inertial reference frame and can be written in integral form as,

$$\frac{\partial}{\partial t}\iiint_V Q\,dV + \iint_S (f\,\hat{i} + g\,\hat{j} + h\,\hat{k})\cdot\hat{n}\,dS = \iint_S (r\,\hat{i} + s\,\hat{j} + t\,\hat{k})\cdot\hat{n}\,dS$$

where

$$Q = \begin{bmatrix} \rho \\ \rho u \\ \rho v \\ \rho w \\ \rho e \end{bmatrix} \quad f = \begin{bmatrix} \rho u \\ \rho u^2 + p \\ \rho uv \\ \rho uw \\ u(\rho e + p) \end{bmatrix}$$

$$g = \begin{bmatrix} \rho v \\ \rho uv \\ \rho v^2 + p \\ \rho vw \\ v(\rho e + p) \end{bmatrix} \quad h = \begin{bmatrix} \rho w \\ \rho uw \\ \rho vw \\ \rho w^2 + p \\ w(\rho e + p) \end{bmatrix}$$

$$r = \begin{bmatrix} 0 \\ \tau_{xx} \\ \tau_{xy} \\ \tau_{xz} \\ a \end{bmatrix} \quad s = \begin{bmatrix} 0 \\ \tau_{xy} \\ \tau_{yy} \\ \tau_{yz} \\ b \end{bmatrix} \quad t = \begin{bmatrix} 0 \\ \tau_{xz} \\ \tau_{yz} \\ \tau_{zz} \\ c \end{bmatrix}$$

$$a = u\tau_{xx} + v\tau_{xy} + w\tau_{xz} + kT_x$$

$$b = u\tau_{xy} + v\tau_{yy} + w\tau_{yz} + kT_y$$

$$c = u\tau_{xy} + v\tau_{yy} + w\tau_{yz} + kT_y$$

A fluid element volume over which the equations are enforced is denoted by V; the bounding surface is denoted S with outward pointing unit normal $\hat{n}$. The Cartesian unit vectors are $\hat{i}$, $\hat{j}$, and $\hat{k}$; ρ is the density; p is the pressure; u, v, and w are the velocity components; e is the specific energy per unit volume; T is the temperature; k is the thermal conductivity; and τ_{xx}, τ_{yy}, τ_{zz}, τ_{xy}, τ_{xz}, and τ_{yz} are the viscous stress tensor components. The ideal gas law closes the system of equations and the entire equation set is non-dimensionalized by freestream density and speed of sound.

Integrating the equations around finite volumes in the domain leads to the semi-discrete form for the system,

$$V_i \frac{dQ_i}{dt} + \sum_{M=1}^{N_i} (f^M \hat{i} + g^M \hat{j} + h^M \hat{k}) \cdot \hat{n}^M S^M = \sum_{M=1}^{N_i} (r\hat{i} + s\hat{j} + t\hat{k}) \cdot \hat{n}^M S^M$$

where the subscripted i and superscripted M denote quantities for the i^{th} cell and the M^{th} face of the cell i, respectively, and N_i is the number of faces bounding cell i. The equations above can be solved on arbitrary cell types in Cobalt. For the current study, unstructured grids containing a combination of tetrahedra and prisms are used. Prisms are used in the boundary layer in order to reduce the number of cells as well as to improve the boundary layer computation. Boundary layer grids comprised of tetrahedra often possess high aspect ratios and can be strongly non-orthogonal. The high aspect ratios create problems in the calculation of divergence of the gradient (Forsythe et al.[17]). Prisms are more orthogonal and place less of a burden on the solver.

For simulation of turbulent flows, the governing equations are suitably averaged, yielding turbulent stresses that require a model. A Boussinesq approximation is invoked in the momentum equations and the turbulent eddy viscosity (μ_t) is used to relate the stresses to the strain rate. The turbulent heat flux is also modeled using a gradient-transport hypothesis, requiring specification of a turbulent thermal conductivity, k_t. Reynolds analogy is applied and the turbulent heat flux is modeled using a constant turbulent Prandtl number of 0.9. Using turbulent eddy viscosity and turbulent conductivity, the variable μ is replaced by $(\mu + \mu_t)$ and k is replaced by $(k + k_t)$ in the governing equations.

Spalart-Allmaras Turbulence Model

The Spalart-Allmaras[13] (SA) one equation model solves a single partial differential equation for a working variable $\tilde{\nu}$ which is related to the turbulent viscosity. The differential equation is derived by "using empiricism and arguments of dimensional analysis, Galilean invariance and selected dependence on the molecular viscosity." The model includes a wall destruction term that reduces the turbulent viscosity in the laminar sublayer. The model takes the form,

$$\frac{D\tilde{\nu}}{Dt} = c_{b1}\tilde{S}\tilde{\nu} - c_{w1} f_w \left[\frac{\tilde{\nu}}{d}\right]^2 + \frac{1}{\sigma}\left[\nabla \cdot ((\nu + \tilde{\nu})\nabla\tilde{\nu}) + c_{b2}(\nabla\tilde{\nu})^2\right]$$

The turbulent kinematic viscosity is obtained from,

$$\nu_t = \frac{\mu_t}{\rho} = \tilde{\nu} f_{v1}, \qquad f_{v1} = \frac{\chi^3}{\chi^3 + c_{v1}^3}, \qquad \chi \equiv \frac{\tilde{\nu}}{\nu}$$

where S is the magnitude of the vorticity given by

$$S = |\omega| = \left|\nabla \times \left(u\hat{i} + v\hat{j} + w\hat{k}\right)\right|,$$

and the modified vorticity is,

$$\tilde{S} \equiv S + \frac{\tilde{\nu}}{\kappa^2 d^2} f_{v2},$$

$$f_{v2} = 1 - \frac{\chi}{1 + \chi f_{v1}},$$

where d is the distance to the closest wall. The wall destruction function f_w is,

$$f_w = g\left[\frac{1 + c_{w3}^6}{g^6 + c_{w3}^6}\right]^{\frac{1}{6}},$$

and

$$g = r + c_{w2}\left(r^6 - r\right), \qquad r \equiv \frac{\tilde{\nu}}{\tilde{S}\kappa^2 d^2}.$$

The turbulent viscosity is obtained from the turbulent kinematic viscosity by $\mu_t = \rho\nu_t$.

The model coefficients are,

$c_{b1} = 0.1355$ $\quad \sigma = 2/3$ $\quad c_{b2} = 0.622$

. $\kappa = 0.41$ $\quad c_{w1} = c_{b1}/\kappa^2 + (1 + c_{b2})/\sigma$ $\quad c_{w2} = 0.3$

$c_{w3} = 2$ $\quad c_{v1} = 7.1$

Approximate SA-Rotation Correction Model

Spalart and Shur[18] presented improvements to the SA model specifically for vortical flows. The modification allows for the production of turbulent viscosity to be reduced in regions of high vorticity. One simple but effective formulation of the rotation correction was presented by Dacles-Mariani et.al.[19]. The modification to SA includes a new destruction term in the modified vorticity based on the magnitude of vorticity and the strain rate. The new modified vorticity is expressed as

$$\tilde{S} \equiv S + \frac{\tilde{\nu}}{\kappa^2 d^2} f_{v2} + C_{vor} \min(0, \hat{S} - S)$$

where S is the magnitude of the vorticity, $\hat{S}$ is the strain rate and C_{vor} is a constant taken to be 4 for all runs. It should be noted that when the strain rate magnitude is ¾ of

the vorticity magnitude, the production term will be essentially zero. This allows vortical, turbulent flows to be calculated with a RANS turbulence model without too much dissipation being added to the vortex core, which typically eliminates the vortex breakdown phenomenon seen in experiments. The SA model with the approximate rotation corrections will be referred to as SARC in the results section.

Menter's Shear Stress Transport Model

Menter's shear stress transport (SST) model is a hybrid $k-\varepsilon$ and $k-\omega$ turbulence model. Typical $k-\omega$ models are well behaved in the near wall region where low Reynolds number corrections are not required. However, they are generally sensitive to the freestream values of ω. On the other hand, $k-\varepsilon$ models are relatively insensitive to freestream values, but behave poorly in the near wall region. Menter proposed a hybrid model. The SST model uses a parameter F_1 to switch from $k-\omega$ to $k-\varepsilon$ in the wake region to prevent the model from being sensitive to freestream conditions. The governing differential equations including a compressibility correction are given by

$$\frac{D(\rho k)}{Dt} = \tau_{ij}\frac{\partial u_i}{\partial x_j}(1-F_1)\overline{p''d''} - \frac{\rho k^{3/2}}{l_{k-\omega}} + \frac{\partial}{\partial x_j}\left[(\mu+\sigma_k\mu_t)\frac{\partial k}{\partial x_j}\right]$$

where $l_{k-\omega} = \dfrac{k^{1/2}}{\beta^*\left[1+\alpha_1 M_t^2(1-F_1)\right]\omega}$

and

$$\frac{D(\rho\omega)}{Dt} = \frac{\gamma\rho}{\mu_t}\tau_{ij}\frac{\partial u_i}{\partial x_j} + (1-F_1)\beta^*\alpha_1 M_t^2\rho\omega^2 - \beta\rho\omega^2 + \frac{\partial}{\partial x_j}\left[(\mu+\sigma_\omega\mu_t)\frac{\partial\omega}{\partial x_j}\right] + 2\rho(1-F_1)\sigma_{\omega 2}\frac{1}{\omega}\frac{\partial k}{\partial x_j}\frac{\partial\omega}{\partial x_j} - (1-F_1)\frac{\overline{p''d''}}{\nu_t}$$

where the pressure dilatation term is

$$\overline{p''d''} = -\alpha_2\tau_{ij}\frac{\partial u_i}{\partial x_j}M_t^2 + \alpha_3\rho\varepsilon M_t^2,$$

and $M_t^2 = \dfrac{2k}{a^2}$ is termed the turbulent Mach number. The closure coefficients for the compressible corrections are

$$\alpha_1 = 1.0 \quad \alpha_2 = 0.4 \quad \alpha_3 = 0.2.$$

Although the current application is at flowfield conditions inconsistent with compressible flow, the compressible corrections were in the SST formulation and have been found to have no effect for very low turbulent Mach numbers. The switching function, F_1, can be computed using

$$F_1 = \tanh\left(\arg_1^4\right),$$

where

$$\arg_1 = \min\left(\max\left(\frac{\sqrt{k}}{0.9\omega y}, \frac{500\mu}{\rho\omega y^2}\right), \frac{4\rho\sigma_{\omega 2}k}{CD_{k\omega}y^2}\right),$$

and

$$CD_{k\omega} = \max\left[2\rho\sigma_{\omega 2}\frac{1}{\omega}\frac{\partial k}{\partial x_i}\frac{\partial\omega}{\partial x_i}, 10^{-20}\right].$$

The switching function also determines the value of the model constants. If ϕ_1 represents a generic constant of the $k-\omega$ equations, and ϕ_2 represents the same constant for the $k-\varepsilon$ equations, then the model constants used in the combined method are determined by

$$\phi = F_1\phi_1 + (1-F_1)\phi_2.$$

The shear stress transport modifications enhance the model's accuracy for separated flows by limiting the turbulent shear stress to $\rho a_1 k$ where $a_1 = 0.31$. The turbulent viscosity is given by

$$\mu_t = \frac{\rho a_1 k}{\max(a_1\omega, \Omega F_2)},$$

where Ω is the absolute value of vorticity. The function F_2 is included to prevent singular behavior in the freestream where Ω goes to zero. F_2 is given by

$$F_2 = \tanh\left(\arg_2^2\right),$$

$$\arg_2 = \max\left(\frac{2\sqrt{k}}{0.09\omega y}, \frac{400\nu}{\omega y^2}\right).$$

The model constants were recalibrated for the shear stress transport modifications and the only change was to σ_{k1}. The following are the coefficients for the hybrid model

Set 1: $(k-\omega)$

$$\sigma_{k1} = 0.85 \quad \sigma_{\omega 1} = 0.5 \quad \beta_1 = 0.0750$$
$$\beta^* = 0.09 \quad \kappa = 0.41 \quad \gamma_1 = \frac{\beta_1}{\beta^*} - \frac{\sigma_{\omega 1}\kappa^2}{\sqrt{\beta^*}}$$

Set 2: $(k-\varepsilon)$

$$\sigma_{k2} = 1.0 \quad \sigma_{\omega 2} = 0.856 \quad \beta_2 = 0.0828$$
$$\beta^* = 0.09 \quad \kappa = 0.41 \quad \gamma_2 = \frac{\beta_2}{\beta^*} - \frac{\sigma_{\omega 2}\kappa^2}{\sqrt{\beta^*}}$$

Detached-Eddy Simulation

Detached-Eddy Simulation (DES) was proposed by Spalart et al.[20]. The motivation for this approach was to combine large-eddy simulation (LES) with the best

features of Reynolds-averaged Navier-Stokes (RANS) methods. RANS methods have demonstrated an ability to predict attached flows very well with a relatively low computational cost. LES methods have demonstrated an ability to compute seperated flowfields accurately but at a tremendous cost for configurations with boundary layers. Spalart's DES method is a hybrid of LES and RANS, which combines the strengths of both methods.

The DES model was originally based on the Spalart-Allmaras one equation RANS turbulence model detailed above with a more detailed presentation in reference [13]. The wall destruction term presented above is proportional to $(\tilde{\nu} / d)^2$, where d is the distance to the wall. When this term is balanced with the production term, the eddy viscosity becomes proportional to $\hat{S}d^2$ where $\hat{S}$ is the local strain rate. The Smagorinski LES model varies its sub-grid scale (SGS) turbulent viscosity with the local strain rate, and the grid spacing : $\nu_{SGS} \propto \hat{S}\Delta^2$, where $\Delta = \max(\Delta x, \Delta y, \Delta z)$. If d is replaced with Δ in the wall destruction term, the S-A model will act as a Smagorinski LES model.

To exhibit both RANS and LES behavior, d in the SA model is replaced by

$$\tilde{d} = \min(d, C_{DES}\Delta).$$

When $d << \Delta$, the model acts in a RANS mode and when $d >> \Delta$ the model acts in a Smagorinski LES mode. Therefore the model switches into LES mode when the grid is locally refined.

DES was first implemented in an unstructured grid method by Forsythe et. al.[21]. They determined the C_{DES} constant should be 0.65, consistent with the structured grid implementation of Shur et. al.[18] when the grid spacing Δ was taken to be the longest distance between the cell center and all of the neighboring cell centers.

Strelets[22] introduced a DES model based on Menter's Shear Stress Transport model. The DES modification to the SST model replaces the length scale, $l_{k-\omega}$, by

$$\tilde{l} = \min(l_{k-\omega}, C_{DES}\Delta)$$

in the dissipative term of the k-transport equation.

A Newton sub-iteration method is used in the solution of the system of equations to improve time accuracy of the point implicit method and approximate Jacobians. In the calculations presented below, a typical number of three Newton sub-iterations is used for all time-accurate cases unless specified in the sub-iteration study.

EXPERIMENTAL METHOD AND FACILITIES

The experimental data used for comparison was obtained by Mitchel et. al.[23] from Onera's F2 wind tunnel. Onera's F2 wind tunnel has a rectangular test section with a width of 1.4m, a height of 1.8m, and a length of 5m. It is powered by a 680kW DC motor that drives a fan with blades spanning 3.15m and provides a maximum free-stream velocity in the test section of 105m/s. A cooling system in the closed-return portion of the wind tunnel facility maintains a constant free-stream temperature in the test section. The relative free-stream velocity, $\Delta U_0/U_0$, is estimated to have an accuracy of 1% while the mean intensity of turbulence has an accuracy of 0.1%.[24]

In F2, the delta wing model depicted in Fig. 3 was mounted on a sting with a horizontal support and flexible joint for adjusting the angle of attack, with an accuracy of ± 0.05°. The horizontal support was manipulated in height along a vertical column so as to maintain the model close to the center axis of the test section. The model was mounted in the test section with no yaw angle with respect to the free-stream flow (estimated accuracy of ± 0.1°). The experimental dataset consists of steady pressure data at many locations on the top side of the delta wing and LDV data in planes parallel to the top surface, perpendicular to the top surface spanwise, and perpendicular to the top surface along the vortex core.

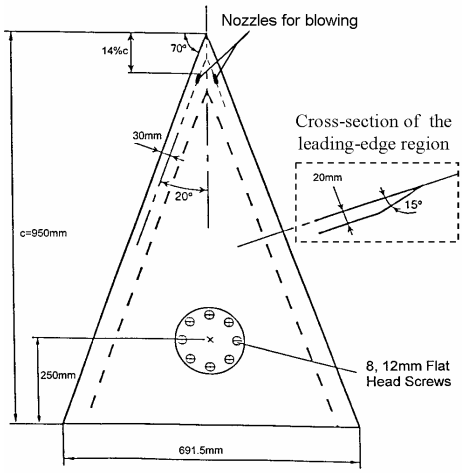

Figure 3: Sketch of the delta wing model with nozzles for along-the-core blowing near the apex.

RESULTS

This section presents results of the numerical simulations, as well as comparison of these simulations to the Onera experimental data set. All cases were run at a freestream velocity of 24 m/s, an angle of attack of 27°, a Mach number of 0.069, and other freestream conditions consistent with a Reynolds number of 1.56 million. No attempt was made to model transition from laminar to turbulent flow on the delta wing. In all cases the spatial and temporal operators were second-order accurate. Fig. 4 depicts a typical time-accurate flowfield solution for SADES. Typical unsteady simulations were run for 9000 time steps with an iteration plus two subiterations per time step. The baseline time step, non-dimensionalized by the root chord and freestream velocity, was 0.005. The delta wing surface is shaded with contours of pressure and an iso-surface of total pressure is depicted to show the primary vortex structure. It is apparent the the simulation was able to both capture the breakdown phenomena as

well as the post breakdown windings typically seen in experiments.

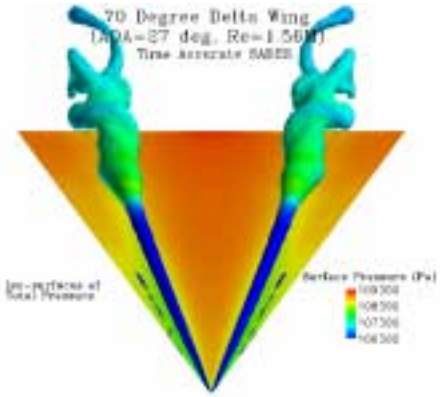

Figure 4: Time-Accurate SADES Solution.

Time Accuracy Study

When computing solutions for unsteady flowfields such as vortex breakdown, it is important to determine the degree to which the solution is time accurate. Fig. 5 depicts the normal force on the delta wing as a function of non-dimensional time for the SADES turbulence model at five different time steps. It is obvious from the figure that this is a very complex flowfield with large variations in time. It is difficult to tell from this figure whether there is a difference in the solutions as time step is varied or simply whether more time is necessary to resolve the resident frequencies and amplitudes of the normal force coefficient.

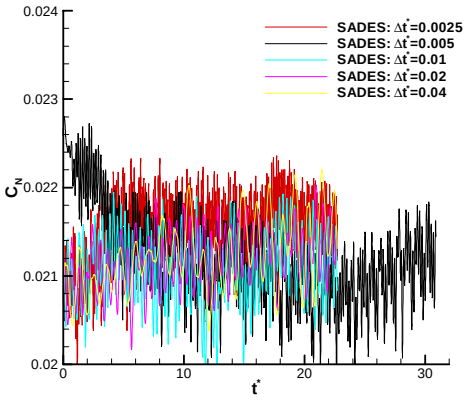

Figure 5: Normal Force Coefficient Time History.

Another way to represent this data is by performing a power spectral density analysis of the time histories. This was accomplished for the current datasets using the MATLAB "psd" function. The psd power was scaled by the number of iterations analyzed and the output frequency was non-dimensionalized by the root chord and freestream velocity, giving the Strouhal frequency, St. To show a coallesence of frequency with time step, the data was plotted versus the inverse of frequency or the wave number. The wave number with the highest power was tracked to determine if there was any change with time step. Fig. 6 shows the behavior of a particular wave number for six variations in time step of SADES. After analyzing the simulation it was determined that the wave number chosen is created by the formation of windings in the post breakdown region. As can be seen in Fig. 6, as the non-dimensional time step is halved the wave number decreases. For the three coarsest time steps, a change in the wave number is approximately equivalent to the decrease in time step. The three most refined time steps rapidly approach an asymptotic value of wave number.

Cobalt also utilizes Newton subiteration to improve time accuracy. In the previous cases, an initial iteration plus two Newton subiterations were performed. To determine the affect of varying the number of subiterations, four different subiteration values were used and the results are presented in Fig. 7.

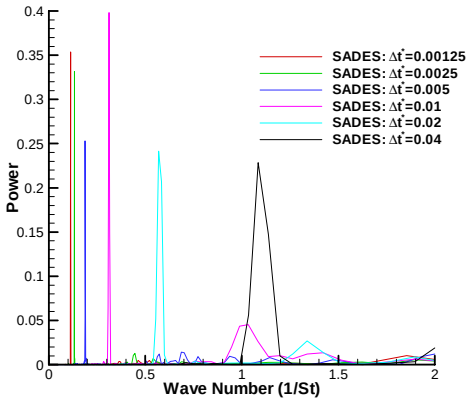

Figure 6: MATLAB power spectral density plot of normal force for variations in time step.

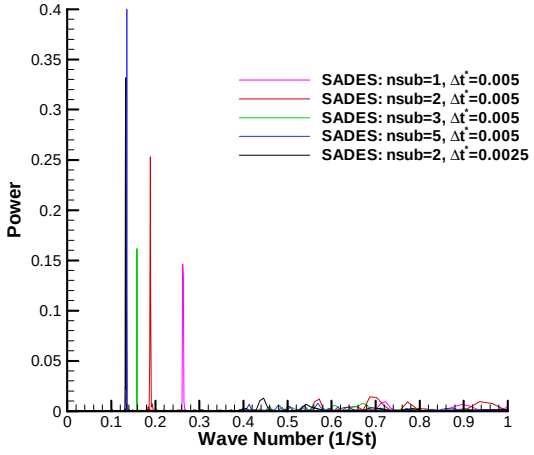

Figure 7: MATLAB power spectral density plot of normal force for variations in subiterations.

Again we can see the wave number is reduced as the number of subiterations is increased. Fig. 8 displays the primary wave number versus the time step and number of subiterations. One can see from the figure that the asymptotic value of this wave number is approximately 0.1

(St=10) and is captured fairly well with the baseline non-dimensional time step of 0.005 and two subiterations. The resulting wave number for the baseline values is 0.188, giving a Strouhal frequency of 5.3. The baseline values of time step and subiteration number were used for the majority of the simulations hereafter.

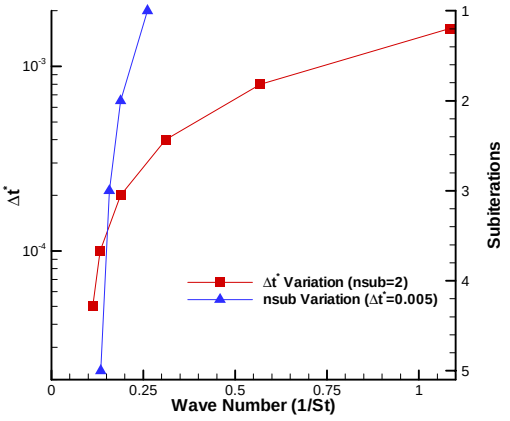

Figure 8: Wave number convergence for a varation in time step and subiteration.

Turbulence Model Study

After determining that the relevant features were being captured by the grid and that a reasonable level of time accuracy was obtained, a study of various RANS and DES turbulence models was accomplished. Fig. 9 depicts the Strouhal frequency versus psd power for the SA, SST, SARC, SADES, and SSTDES turbulence models. All were run for 9000 iterations from a well developed SADES solution. Transients from the initiation of the turbulence model were eliminated from the datasets analyzed by not incorporating the first 1000 iterations in the frequency analysis.

Several conclusions can be made from Fig. 9. First, the SA and SST RANS models used widely by the industry are not able to capture the majority of the frequencies in the spectrum. In the case of both RANS models, all frequencies, except the dominant frequency previously discussed, have a power one could reasonably associate with random noise. Next, the SARC model compares surprisingly well with the DES methods. This is most likely due to the fact that the rotation correction is very effective in eliminating the affects of turbulence dissipation in the core of the vortex. The only range of frequencies the SARC model is not able to capture as well as the DES methods is 3<St<5, where the power is not as high as the DES methods. Finally, both DES methods are able to capture the full range of frequencies resident in the simulation of delta wings at high angles of attack. One further note concerning the SARC model is the fact that although it is able to capture the high Reynolds number vortex breakdown phenonmenon fairly well, the simulation has little hope of improving with a refinement in grid as is the case with the DES methods. Also, SARC is only an improvement in typical RANS models for vortical flows. Simulations with either DES method can improve with grid refinement, due to their LES nature, and also simulate massive separation not associated with strong vortices.[22]

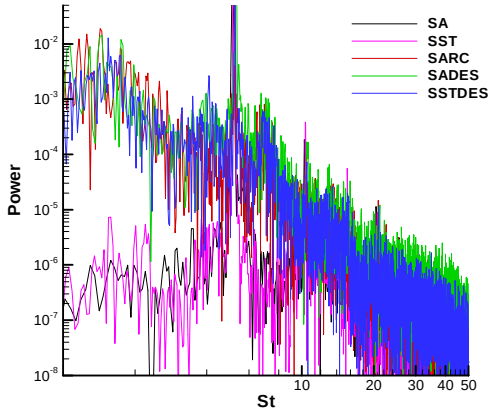

Figure 9: MATLAB PSD for Various Turbulence Models.

Fig.s 10-13 depict the flowfields for all of the turbulence models except the SST RANS model. The SST RANS model is not present since there is no visible difference between it and the SA RANS model. Note the lack of vortex breakdown for SA (and SST as well) commonly seen in experiments. Also, note the difference in winding characteristics between the SARC method and both DES methods. In the SARC simulation, as the vorticies lose their coherence, the correction is less likely to activate.

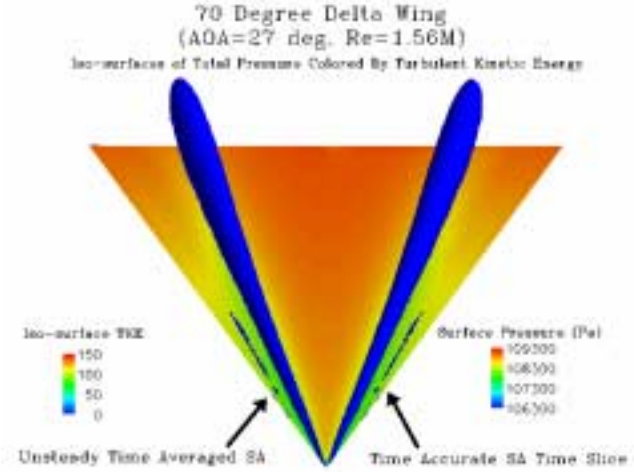

Figure 10: Spalart-Allmaras RANS Simulation

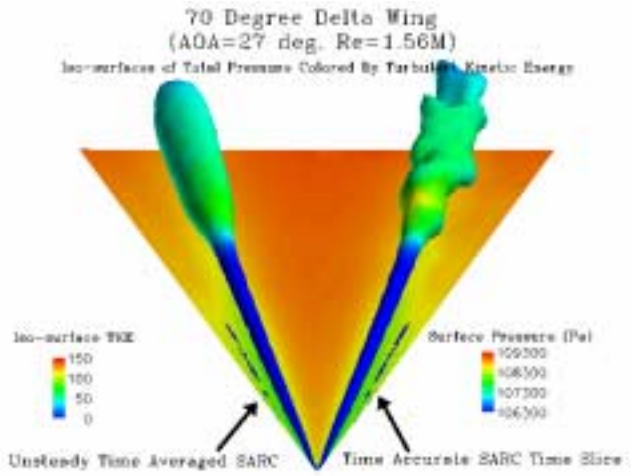

Figure 11: SARC RANS simulation.

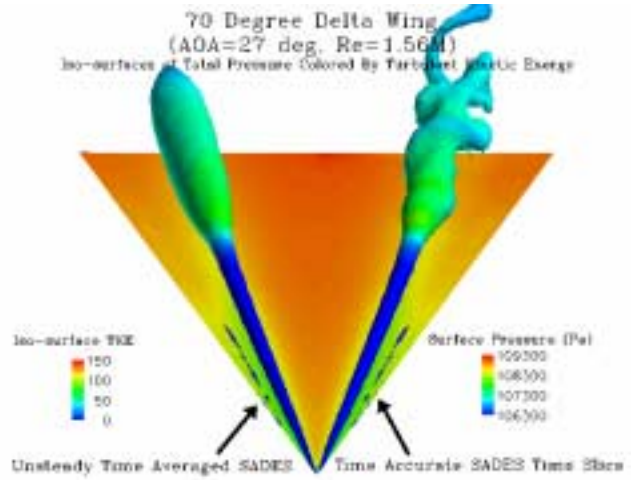

Figure 12: SA-Detached Eddy Simulation.

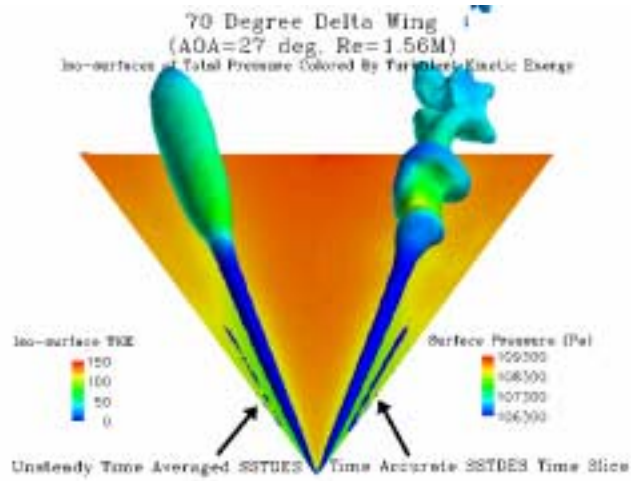

Figure 13: SST-Detached Eddy Simulation.

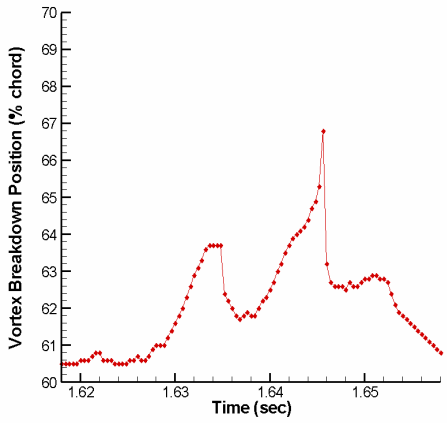

Figure 14: SADES Vortex breakdown position with time (u=o).

Comparison with Experiment

The experimental data of Mitchel et. al.[23] was next used to determine the degree to which SADES and the other models matched the experiments. A set of SADES time slices were interrogated to determine the vortex breakdown position as a function of time for several cycles of the primary frequency. Fig. 14 displays the vortex breakdown position, as determined by a stagnation point along the core, as a function of time. The vortex breakdown position range of motion is $0.605<x/c<0.67$. Over the period examined, the position is aperiodic and experiences abrupt changes due to the formation and elimination of stagnation bubbles during the simulation. Fig. 15 is a summary of the vortex breakdown position as a function of angle of attack, as seen experimentally by Mitchel et. al.[23]. The numerically computed vortex breakdown is in excellent agreement with the experimental results at 27^o angle of attack, falling within the range of uncertainty.

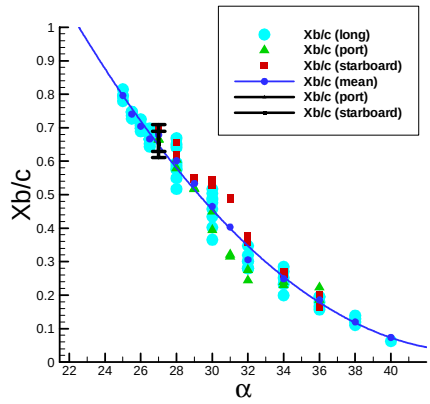

Figure 15: Experimental vortex breakdown position.

Next, Fig. 16 (a-d) depicts cross-planes of vorticity for SADES and the experiment at four distances along the root chord.

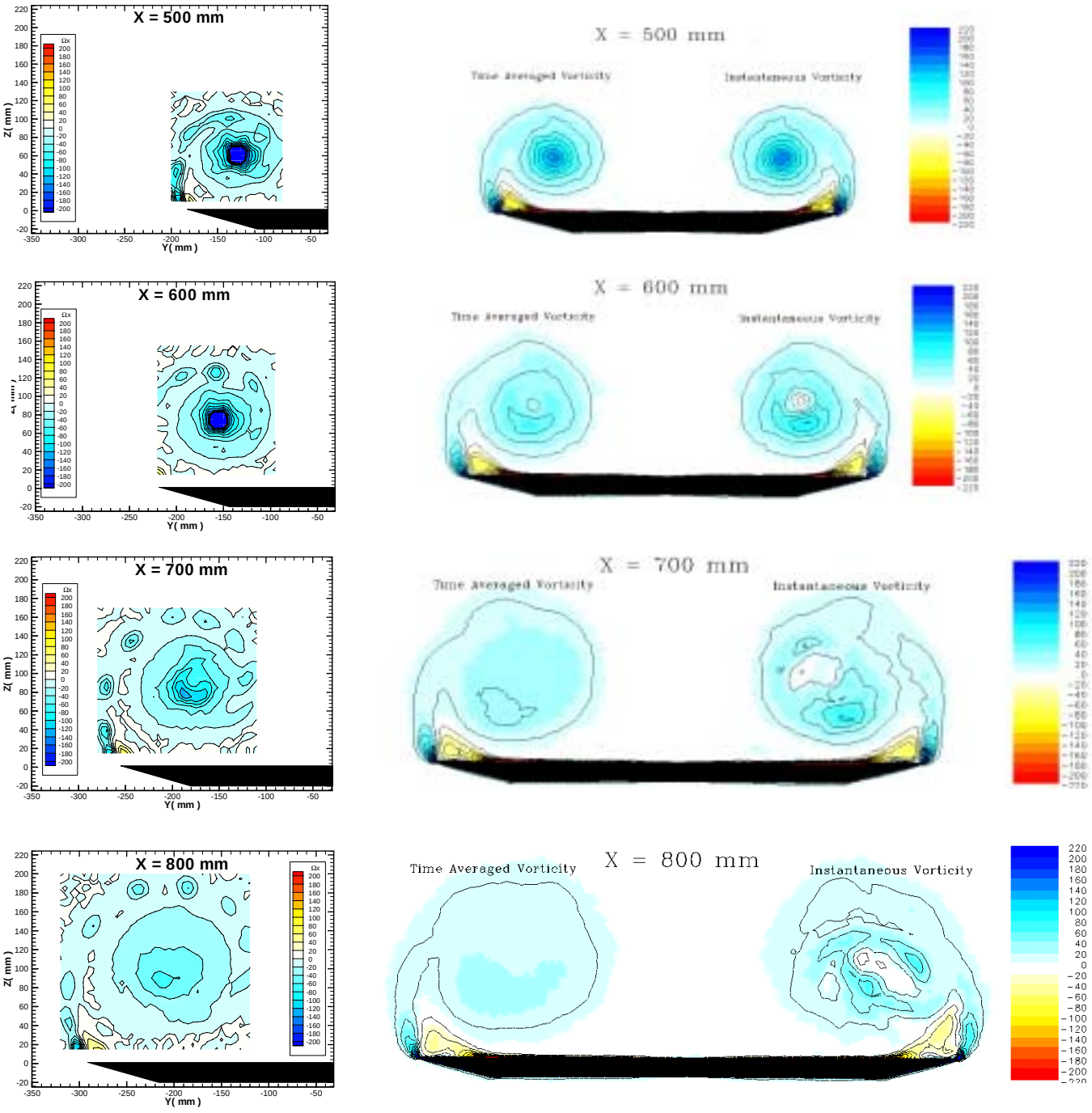

Figure 16: Vorticity in various crossplanes comparison between the ONERA experimental data and SADES.

At each cross-plane station, the scale and color maps are consistent with the experiment. The time average of vorticity over the entire simulation is displayed on the left half of the delta wing and the instantaneous vorticity is displayed on the right half of the delta wing. It is readily apparent that the geometry of the vortex and the relative strength of vorticity are in good agreement with the numerical simulations for both the primary and secondary vortex. The experiment has a moderately higher value of vorticity in the core as seen by the darkness of the blue shading in the core region. It should be noted that at the 600 mm station, the experiment shows breakdown has not occurred but the simulation shows it has broken down. The flowfield was interrogated to determine the vortex breakdown position for this instant in time and it is at 590 mm, explaining the difference in this cross-plane vorticity. It should also be noted that the experiment was not able to gather vorticity data very close to the surface, due to experimental limitations, whereas the simulation captured both the vorticity in the boundary layer and the secondary vortex. The 700 mm and 800 mm experimental cross-plane figures show evidence of the secondary vortex at the same vorticity level and position as the numerical simulations.

To determine if the production of turbulent kinetic energy is equivalent with the experiment, cross-planes of resolved turbulent kinetic energy in a horizontal plane through the vortex core were examined and compared to the experiment. As in the previous comparisons, careful attention was paid to matching the color maps and geometry of the experimental data. The figures based on numerical simulation have a black line located at the delta wing leading edge for reference.

It is clear from Fig.'s 17 and 18 that RANS models add too much turbulent eddy viscosity to the core of the vortex, which in turn kills the resolved turbulent kinetic energy. This is the reason that typical RANS models can not reproduce vortex breakdown very well. Fig. 19 demonstrates the affects of the rotation correction in the SARC model. In the core of the vortex the vorticity magnitude dominates the strain rate, creating a turbulent eddy viscosity destruction term in the region of the vortex. The lack of eddy viscosity allows a highly energetic burst. As can be seen in Fig. 19, the turbulent kinetic energy contours are very similar to the experiment. The major disagreement is in the location of the breakdown.

Both DES models are also able to capture the turbulent kinetic energy patterns in the experimental data as can be seen in Fig.'s 20-21. Although the level of turbulent kinetic energy found in the cross plane is lower than that found in the experiment, the region of increased turbulent kinetic energy has a very similar shape and the location of vortex breakdown is closer to the experiment. Two things should be noted with respect to the DES models. First, SSTDES is closer to the experiment than SADES for a given time step. Also, when the time step used to compute the SADES solution is decreased by a factor of four, the solution is much closer to the experiment. This is consistent with the fact that DES is an LES based method and will improve with a reduction in time step or grid cell size. It would be instructive to see how a SARC based DES method would compare to the experiments and other turbulence methods.

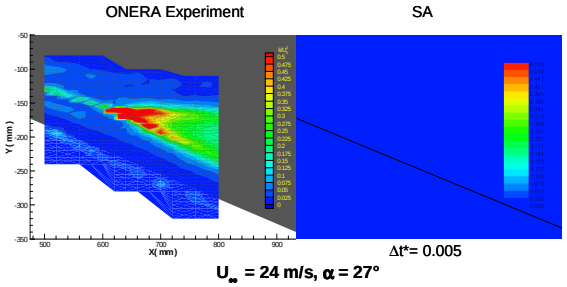

Figure 17: SA and experimental turbulent kinetic energy in a horizontal plane through the vortex core.

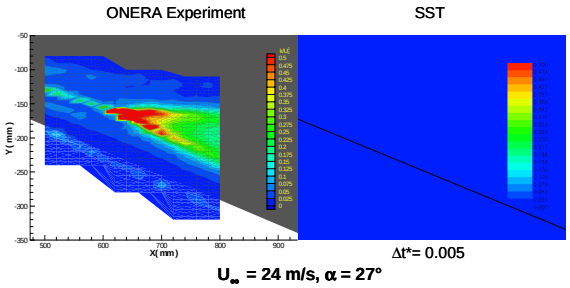

Figure 18: SST and experimental turbulent kinetic energy in a horizontal plane through the vortex core.

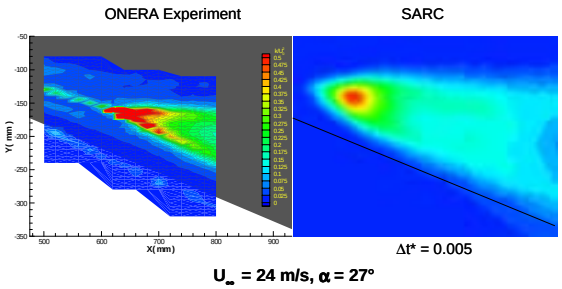

Figure 19: SARC and experimental turbulent kinetic energy in a horizontal plane through the vortex core.

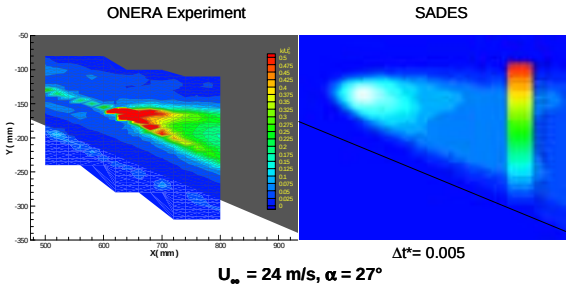

Figure 20: SADES and experimental turbulent kinetic energy in a horizontal plane through the vortex core.

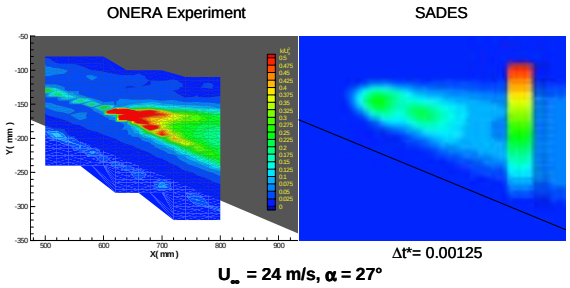

Figure 21: SADES and experimental turbulent kinetic energy in a horizontal plane through the vortex core at a refined time step.

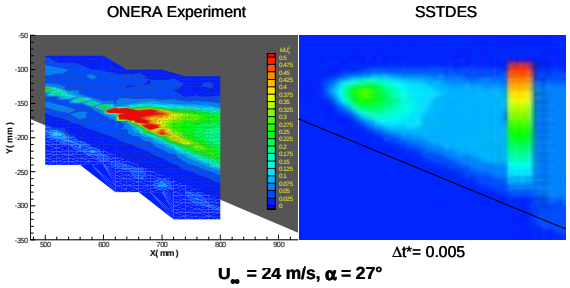

Figure 22: SSTDES and experimental turbulent kinetic energy in a horizontal plane through the vortex core.

The last comparison with experiment demonstrates the ability of DES methods to accurately reproduce the flowfield near the surface. Fig. 23 depicts experimental and numerically derived surface oil patterns. It is not surprising that SA and SADES give essentially the same solution since DES acts in RANS mode near the surface. It is encouraging to note that the oil patterns compare very well with the experiment. The major difference is the inability of the computations to represent the "pinching" of the paterns near the leading edge at the 40% x/c station. This behavior is most likely due to a transition from laminar to turbulent flow and was not reproduced in the computations since there was no transition model implemented for any of the computational methods.

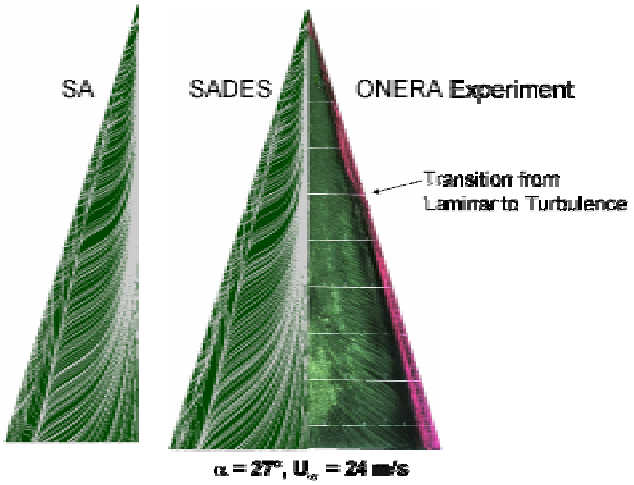

Figure 23: Oil flow comparison between SA, SADES and experiment.

CONCLUSIONS AND RECOMMENDATIONS

DES simulations of a delta wing experiencing vortex breakdown were successfully computed and compared to RANS methods and a very detailed experiment. These solutions were shown to be sensitive to time accuracy in the frequency domain but achieved an asymptotic solution as time step was reduced. The typical RANS methods of SA and SST were shown to be inadequate in capturing the physics of vortex breakdown at high Reynolds number, whereas, both DES methods and SARC captured the full spectrum of frequencies and compared very well with the experimental data.

The success of SARC near the vortex breakdown position motivates the inclusion of a rotation correction within the DES method. The turbulent eddy viscosity will go to zero for DES as the grid is refined, approaching a direct numerical simulation. Adding the rotation correction to DES would potentially allow a reduction in the turbulent eddy viscosity prior to the breakdown location on moderate grids. The success of DES in capturing the windings would be maintained. In summary, the overall success of DES methods in capturing vortical flows, combined with the previous success in capturing massively separated flows, make them extremely useful for full aircraft solutions at high angles of attack and flight Reynolds numbers.

Future research should incorporate a very detailed grid convergence study coupled with a complete time-accuracy study to determine the necessary grid and temporal resolution of DES methods when computing vortical flowfields. In addition, a DES modified SARC method should be investigated to determine the advantages and disadvantages for the full range of applications.

∗ **Associate Professor, Associate Fellow AIAA.**

& Assistant Professor, Member AIAA.
φ Assistant Professor, Member AIAA.

∞ USAF Academy Cadet Aero Major.

[1] Werlé, H., "Quelques résultats expérimentaux sur les ailes en flèche, aux faibles vitesses, obtenus en tunnel hydrodynamique" *La Recherche Aéronautique*, No. 41, Sep.-Oct. 1954, pp. 15-21.

[2] Peckham, D.H., Atkinson, S.A., "Preliminary Results of Low Speed Wind Tunnel Tests on a Gothic Wing of Aspect Ration 1.0", Aeronautical Research Council Technical Report, C.P. No 508, T.N. Aero 2504, Apr. 1957.

[3] Elle, B.J., "An Investigation at Low Speed of the Flow near the Apex of Thin Delta Wings with Sharp Leading Edges", Aeronautical Research Council R&M, No. 3176, 1961.

[4] Lambourne, N.C., Bryer, D.W., "The Bursting of Leading-Edge Vortices-Some Observations and Discussion of the Phenomenon", Aeronautical Research Council R&M No. 3282, 1962.

[5] Hall, M.G., "Vortex Breakdown*", Annual Review of Fluid Mechanics*, Vol. 4, 1972, pp. 195-218.

[6] Leibovich, S., "The Structure of Vortex Breakdown," *Annual Review of Fluid Mechanics*, Vol. 10, 1978, pp. 221-46.

[7] Sarpkaya, T. "On Stationary and Traveling Vortex Breakdowns," *Journal of Fluid Mechanics*, Vol. 45, Part 3, 1971, pp. 545-559.

[8] Nelson, R.C., "Unsteady Aerodynamics of Slender Wings," Aircraft Dynamics at High Angles of Attack: Experiments and Modeling, AGARD-R-776, 1991, pp.1-1 to 1-26.

[9] Délery, J., "Aspects of Vortex Breakdown," *Progress in Aerospace Sciences*, Vol. 30, 1994, pp. 1-59.

[10] Faller, J.H., Leibovich, S., "Disrupted states of vortex flow and vortex breakdown", *Physics of Fluids*, Vol. 20, No. 9, 1977, pp.1385-1400.

[11] Menke, M., Yang, H., Gursul, I., "Further Experiments on Fluctuations of Vortex Breakdown Location," AIAA-96-0205, 34th AIAA Aerospace Sciences Meeting and Exhibit, Jan 1996, Reno, NV.

[12] Mitchell, A.M., Molton, P., Barberis, D., Délery, J., "Oscillation of Vortex Breakdown Location and Control of the Time-Averaged Location by Blowing," *AIAA Journal*, Vl. 38, No. 5, May 2000, pp.793-803.

[13] Spalart, P. R., and Allmaras, S.R., "A One Equation Turbulence Model for Aerodynamic Flows," *La Recherche Aerospatiale*, 1994, 1, p.5.

14 Strang, W.Z., Tomaro, R.F., Grismer, M.J., "The Defining Methods of Cobalt: A Parallel, Implicit, Unstructured Euler/Navier-Stokes Flow Solver," AIAA 99-0786, January 1999.

[15] Samareh, J., "Gridtool: A Surface Modeling and Grid Generation Tool," Proceedings of the Workshop on Surface Modeling, Grid Generation, and Related Issues in CFD Solution, NASA CP-3291, May 9-11, 1995.

[16] Pirzadeh, S., "Progress Toward A User-Oriented Unstructured Viscous Grid Generator," AIAA Paper 96-0031, January 1996.

17 Forsythe, J.R., Strang, W.Z., and Hoffmann, K.A., "Validation of Several Reynolds-Averaged Turbulence Models in a 3-D Unstructured Grid Code," AIAA 00-2552, June 2000.

18 Spalart, P.R., and Shur, M.L., "On the Sensitization of Turbulence Models to Rotation and Curvature," *Aerospace Science and Technology*, 1997.

19 Dacles-Mariani, J., Zilliac, G.G., Chow, J.S. and Bradshaw, P., "Numerical/experimental study of a wingtip vortex in the near field", AIAA Journal, vol. 33, no. 9, pp. 1561-1568, 1995.

20 Spalart, P. R. , Jou W-H. , Strelets M. , and Allmaras, S. R., "Comments on the Feasibility of LES for Wings, and on a Hybrid RANS/LES Approach," *Advances in DNS/LES, 1st AFOSR Int. Conf. on DNS/LES*, Aug 4-8, 1997, Greyden Press, Columbus Oh.

21 Forsythe, J.R., Hoffmann, K.A., Dieteker, F.F., "Detached-Eddy Simulation of a Supersonic Axisymmetric Base Flow with an Unstructured Flow Solver," AIAA 00-2410, June 2000.

22 Strelets, M., "Detached Eddy Simulation of Massively Separated Flows," AIAA 01-0879, January 2001.

23 Mitchell, A., Molton, P., Barberis, D., and Delery, J., "Characterization of Vortex Breakdown by Flow Field and Surface Measurements," AIAA 2000-0788, January 2000.

[24]

ACKNOWLEDGEMENTS

The authors would like to express our thanks to AFOSR/NI for their support in the Windows on Europe Program. We would also like to thank the Maui Major Shared Resource Center for their generous support.